

Supplementary Information for

“Diagenesis is key to unlocking outcrop fracture data suitable for quantitative extrapolation to geothermal targets”

S. J. Elliott et al. (2025)

Table of Contents

2. Supplementary Methods	Page 2
2.1 Microstructural Image Acquisition	Page 2
2.2 Rock Mechanical Properties	Page 3
2.3 1D and 2D Size and Spatial Arrangement and Connectivity	Page 3
4. Supplementary Results	Page 4
4.1 Sandstone Properties	Page 4
IGV and Pressure Solution	Page 4
<i>Supplementary Figure S1</i> – Schmidt Hammer Compressive Strength	Page 5
4.3.2 Quartz and other Cements	Page 7
Fe-oxide Cement	Page 7
4.3.4.2 Kinematic Aperture Size, Predictive Spacing, and Emergent Threshold	Page 7
<i>Supplementary Table S1</i> – Aperture Best-fit Chi Square Values	Page 7
4.3.5 Spatial Arrangement	Page 7
4.3.5.1 Fracture Spacing	Page 7
<i>Supplementary Figure S2</i> – 2D NCC Spatial Arrangement, Rt16	Page 8
<i>Supplementary Figure S3</i> – Location of BR Outcrop Scanlines	Page 9
<i>Supplementary Figure S4</i> – BR Scanline 1 data	Page 10
<i>Supplementary Figure S5</i> – BR Scanline 2 data	Page 10
<i>Supplementary Figure S6</i> – Fracture Clustering & Paleoflow	Page 11
4.3.6 Fluid Inclusion Microthermometry	Page 11
<i>Supplementary Table S2</i> – Set A FIA Microthermometric Results	Page 12
References	Page 13

2 Supplementary Methods

2.1 Microstructural image acquisition

We document rock and fracture deposit mineralogy and textures using transmitted light microscopy, SEM cathodoluminescence imaging (SEM-CL), and variable pressure secondary electron imaging (VPSE) that reveals textures and quartz luminescence intensities and colors reflecting trace elements and mineral lattice defects (Götze et al., 2001; Stokes, 2008). Polished thin sections were carbon-coated (25 nm) and imaged using a Zeiss Sigma Field Emission Scanning Electron Microscope (FE-SEM) with Gatan MonoCL4 cathodoluminescence (CL) detector, Oxford X-max 50 Silicon Drift X-ray Energy Dispersive Spectroscopy (EDS) detector, and a variable pressure secondary electron detector (VPSE) for charge-contrast imaging (CCI). FE-SEM software allows large-area ($>1 \text{ mm}^2$) automated mosaic construction. SEM-CL working conditions were 6 kV, 120 μm aperture, high current, 150 μs dwell time, and spatial resolution of $\sim 100\text{-}350 \text{ nm}$ per pixel depending on magnification. EDS imaging used 10 kV and a 200 μs dwell time and VPSE, 20 kV, 50 μs dwell time, and a 2 μm pixel resolution. Color CL is accomplished by combining images collected with RGB filters. RGB color balance and contrast were adjusted using image-processing software.

In JMicrovision® we point counted correlative image stacks (SEM-CL and EDS). Varying image layer transparency in JMicrovision® allowed sub-micron scale, quantitative determination of mineral composition or porosity at each grid point; a minimum of 800 points per imaged area produces 99% confidence that all mineral constituents were counted within 95% of their true proportions (Thompson, 1987). A plateau in compositional variability graphs generated within JMicrovision® shows that ~ 1000 total points per imaged area is sufficient. Area mosaics for point counts combine SEM-CL and EDS, aiding discrimination of detrital and cement abundances; EDS provides semi-quantitative composition maps. Point count categories include detrital quartz, detrital K-feldspar, calcite, accessory minerals (zircon, titanium-oxides, apatite), iron-oxides, quartz cement, feldspar cement, illite, kaolinite, primary porosity, and secondary porosity.

For recording microfracture populations, strip-shaped multi-thin section image mosaics collected primarily using panchromatic SEM-CL images (gray-scale intensities) comprise multiple rows, with magnifications ranging from $175\times$ to $250\times$ depending on grain size (wider strip for coarse-grained rock). Most sections are cut parallel to bedding to maximize sampling of steeply dipping fractures, but some were cut normal to bedding to corroborate dips.

Fluid inclusion assemblage microthermometry was performed using a Fluid, Inc.–adapted, U.S. Geological Survey–type, gas-flow heating-freezing stage mounted on an Olympus BX51 microscope with a $40\times$ objective (numerical aperture [NA] = 0.55) and $15\times$ oculars. The gas-flow stage was calibrated using synthetic H_2O and $\text{H}_2\text{O-CO}_2$ fluid inclusions to the critical temperature of H_2O (374.1°C), melting temperature of H_2O ice (0°C), and the melting of dry ice (-56.6°C),

respectively. Homogenization and ice melting temperatures were measured with a precision of 0.1°C. Two-phase aqueous fluid inclusion assemblages at room temperature were heated to homogenization (T_h) to single-phase liquids (Goldstein and Reynolds, 1994; Fall and Bodnar, 2018) and minimum trapping temperatures (T_t) were inferred. Microthermometry was performed before SEM-CL imaging to avoid possible beam damage to fluid inclusions.

2.2 Rock mechanical properties

In situ rock mechanical properties were tested using an N-type Silver Schmidt Hammer that allows rapid non-destructive measurement of rebound of a spring-loaded mass impacting against the outcrop surface. Rebound values are typically referenced against a conversion chart to determine a rock's compressive strength (Aydin and Basu, 2005; Katz et al., 2000), however the digital Silver Schmidt automatically calculates compressive strength values from rebound values recorded in newtons per square millimeter (N/mm^2) ($1 \text{ N}/\text{mm}^2 = 1 \text{ MPa}$). Measurements were taken at 10 localities including deformation bands, sandstone adjacent to bands, and sandstone far from bands with qualitatively different fracture patterns. 10 – 16 tests were conducted within the same bedding horizon per locality. See Supplementary Image 1 and Supplementary Table 3 for details.

2.3 1D and 2D size and spatial arrangement and connectivity

We describe fractures based on maps and scanlines. Scanlines record location and size (kinematic aperture, length) for intersecting fractures along one-dimensional survey lines. To reduce bias and orientation artifacts, scanlines were oriented at a high angle to fracture strike for each set. True inter-fracture distances were measured and corrected using trigonometric corrections (Terzaghi, 1965). Kinematic apertures (opening displacements or widths) (Wennberg et al., 2016) were measured using a comparator having logarithmically graduated stripes for width-binning (Ortega et al., 2006). For microstructural analysis we used continuous bed-parallel multi-thin section microscanlines from oriented samples (Gomez and Laubach, 2006). We characterized 1D spatial arrangement with coefficient of variation (C_v) (Gillespie et al., 2001; Hooker et al., 2023b) and open-access *CorrCount* software for normalized correlation count (NCC) metrics (Marrett et al., 2018). NCC estimates how close a fracture pattern is to a random arrangement by calculating the distances between fractures and comparing them with randomizations (Marrett et al., 2018). The results are validated with a statistical envelope obtained from randomizations.

Two-dimensional fracture distribution data was acquired from a texture-shaded 1-m LiDAR bare earth digital terrain model (DTM) (Allmendinger pers comm. 2022; Allmendinger & Karabinos, 2023), with a camera-equipped Mavic Pro 2 drone flown at 20 to 30 m elevation covering areas of as much as 0.2 km², from iPhone 12 Pro 1-2 m elevation LiDAR (Scaniverse,

Polycam, and 3dScanner software) covering 40 to 1000 m², and from high-resolution photomontages with SEM-CL covering as much as 3800 mm². Drone flight paths were planned using DJI Pilot software. Drone Deploy software was used to build stitched orthorectified mosaics which were then processed in ArcGIS to acquire length, orientation, and fracture center point (barycenter) position data. For Set A fractures at one outcrop, two-dimensional spatial arrangement patterns were analyzed with the 2D correlation count method using barycenter position and weights by length or strike (Corrêa et al., 2022). For the 1-m LiDAR bare earth digital terrain model (DTM), a technique called texture shading was used which emphasizes the derivative of the slope by passing the data through a fractional Laplacian Operator (like a partial edge detector) (Allmendinger & Karabinos, 2023). The practical effect of this processing is two fold: (a) it eliminates the bias imposed by artificial illumination and (b) concave up topography appears dark (darker values indicate more extreme concave curvature) and convex up topography is light. Because the last returned reflections from the LiDAR pulse are used to produce the “bare earth” DEM, this method of processing allows the imaging of surface variation caused by underlying structure and bedding even in areas that are completely vegetated and even those that have a relative thin soil cover. In the Altona area, both the bedding and the macroscopic fractures in the Potsdam are spectacularly well imaged by the texture shading processing technique.

Trace lengths, intersections, and terminations were mapped at specific scales using a magnification where image pixels are visible. We analyzed trace patterns with FracPaQ2D (Healy et al., 2017) and ArcGIS. For network connectivity and length analysis, terminations were classified using isolated (I) and connected nodes (Y and X) (e.g., Sanderson and Nixon, 2015) and scale-dependent rule-based contingent (C) nodes (Forstner and Laubach, 2022) that identify diagenesis-sensitive connections and continuity.

4 Supplementary Results

4.1 Sandstone Properties

IGV & Pressure Solution

Intergranular volume (IGV) was calculated as the sum of intergranular porosity, intergranular authigenic cement, and matrix (e.g., Paxton et al., 2002). IGV is an indirect marker of compaction that typically diminishes from initial values of c. 40 % to less than 30% at depths of ~1500 m (Lander and Walderhaug, 1999). In our samples, IGV averages 22% and ranges from 20.8 to 23.4% (Table 2). Assuming an initial IGV of 40%, compactional porosity loss (COPL) is 23% and cementational porosity loss (CEPL) is 16%. The ratio of compactional porosity loss to total porosity loss is 0.59 (Milliken et al., 2005). Because the Potsdam is a clean (minor feldspar, no lithics), uniform, rigid and densely packed rock (Fig. 3), pressure solution must have played a

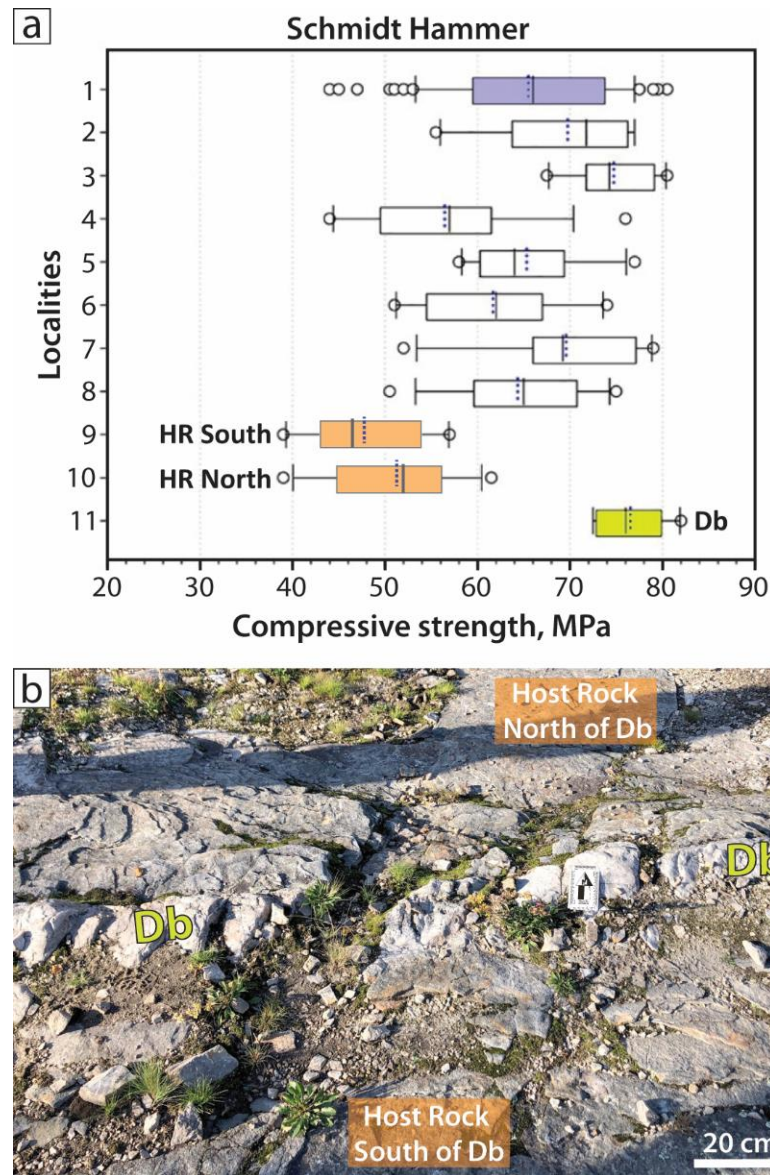
role along with mechanical grain rearrangement for the Potsdam to have reached 22% IGV (Lundegard, 1992).

A component of solutional IGV loss was observed but not quantified. Grain contact solution boundaries range from point to curvilinear to well-developed sutured penetrations (Fig. 3c, d). Stylolitic boundaries occur at ~52% of grain contacts, locally 45% - 63%, and as much as 10% of quartz grains have evidence of fracture from grain-grain contacts, reflecting a component of compaction by chemical dissolution and brittle deformation (e.g., Milliken and Laubach, 2000). Quartz cement in grain-contact fractures was not accounted for in point counts but is probably no more than 0.5% of the total rock volume.

Stylolites parallel to beds mark grain interpenetration by chemically assisted local dissolution and bed-normal shortening. A few steeply dipping, north-south striking bed-normal stylolites form a widely spaced cleavage and record local, minor (c. 0.1%) solution-enhanced east-west shortening. Steeply dipping interdigitated (solution) contacts on individual grains mostly strike north-south, but the pattern is indistinct with subsidiary NE and NW trends. Interdigitated ~E-W boundaries account for only ~8% of grain boundaries measured.

Low IGV values are compatible with quartz and feldspar accumulation in primary pore space likely postdating most compaction, but quartz-filled fractures and stylolitic, interdigitated grain contacts mark compaction (and lateral, tectonic shortening) broadly contemporaneous with some cement deposits. Mutually penetrating/overlapping quartz and feldspar cement is compatible with coeval precipitation in Potsdam sandstone as noted elsewhere (Kastner and Siever, 1979; Selleck, 1997).

Schmidt Hammer Compressive Strength Results



Supplementary Figure S1. Schmidt hammer rebound compressive strength versus locality, BR (n=113 total tests). **(A)** Box plot, median (solid vertical bar), mean (dotted, blue) interquartile range (box), data values 1.5 times interquartile range (whiskers), and outliers (dots). L1, all combined measurements not in or near deformation bands (n=81, mean 65.5 MPa). L2-3, rock with fracture sets in regular chessboard pattern (mean 72.3 MPa; range 55.5 – 80.5 MPa). L4-5, rock with fracture cluster (mean 56.5 MPa; range 44 – 76 MPa). L6-7, rock with sparse fractures separated by >2 m distance (mean 65.0 MPa; range 50.5 – 79 MPa). L8, rock with iron-stained fracture cluster (mean 65.3 MPa; range 58 – 77 MPa). L9-10, unfractured rock directly south (mean 47.8 MPa, n=10) and north (mean 51.3 MPa, n=12) of deformation band (avg. 49.5 MPa; total range 39 – 61.5 MPa). L11, Deformation band (76.5 MPa; std. dev. 3.5 MPa; range 72.5 – 82 MPa). Compressive strength N/mm^2 ; $1 \text{ N}/\text{mm}^2 = 1 \text{ MPa}$. **(B)** BR outcrop showing 100 mm wide deformation band (Db) and unfractured host rock to the North and South. North arrow card is against band.

4.3.2 Quartz and Other Cements

Fe-Oxide cement

A survey of stain occurrence along three scanlines from Rt16 (Fig. 11a; Table 3) reveals that among Set A fractures, about 8% have some iron stain within the fracture (16 out of 211; Rt16-1a). Most of these are clustered to the west of the scanline (red line in Fig. 11a), with only two stained fractures on the eastern side of the scanline. No Set B fractures were intersected, while 12.5% of Set C (3 out of 24; Rt16-2) and 3.5% of Set D (2 out of 57; Rt16-3) have staining. Stains were also surveyed on two ~E-W oriented scanlines capturing Sets A-C at BR (Figs. 11c, 14g). Scanline BR-2 found 54% of surveyed fractures have stain (133 out of 246), most along Set A fractures (121 out of 133). For Scanline BR-1, 36% of fractures have stains (62 out of 171).

4.3.4.2 Kinematic Aperture Size, Predictive Spacing, and Emergent Threshold

Supplementary Table S1 – Microfracture Aperture Best-fit Chi Square Values

MicroScanline	Fracture Set Measured	N	Scanline Length (mm)	Power Law*	Exponential	Normal	Lognormal
R16-3-2C-1	A	181	42.15	4.7913	159.7057	Inf	1502.921
	C	66		4.5933	13.6436	4.69E+10	858.3883
R13-3-2C-2	D	80	44.11	5.7936	6.6906	1906755.2	3.6469
R16-3-2B	A	243	41.19	7.5123	254.5954	Inf	215.7559
BR-21-3	A	45	20.11	1.3351	6.2074	56.5353	4.2053
	B	40		4.2916	1.2569	1.2654	0.21618
	C	30		2.8642	0.776	0.80167	0.22406
RR-4	A	31	34.30	1.3082	0.5101	0.20922	0.1626
	B	92		20.4865	7.2446	1.1103	0.35905
	C	126		26.4422	3.0196	40.8906	1.177

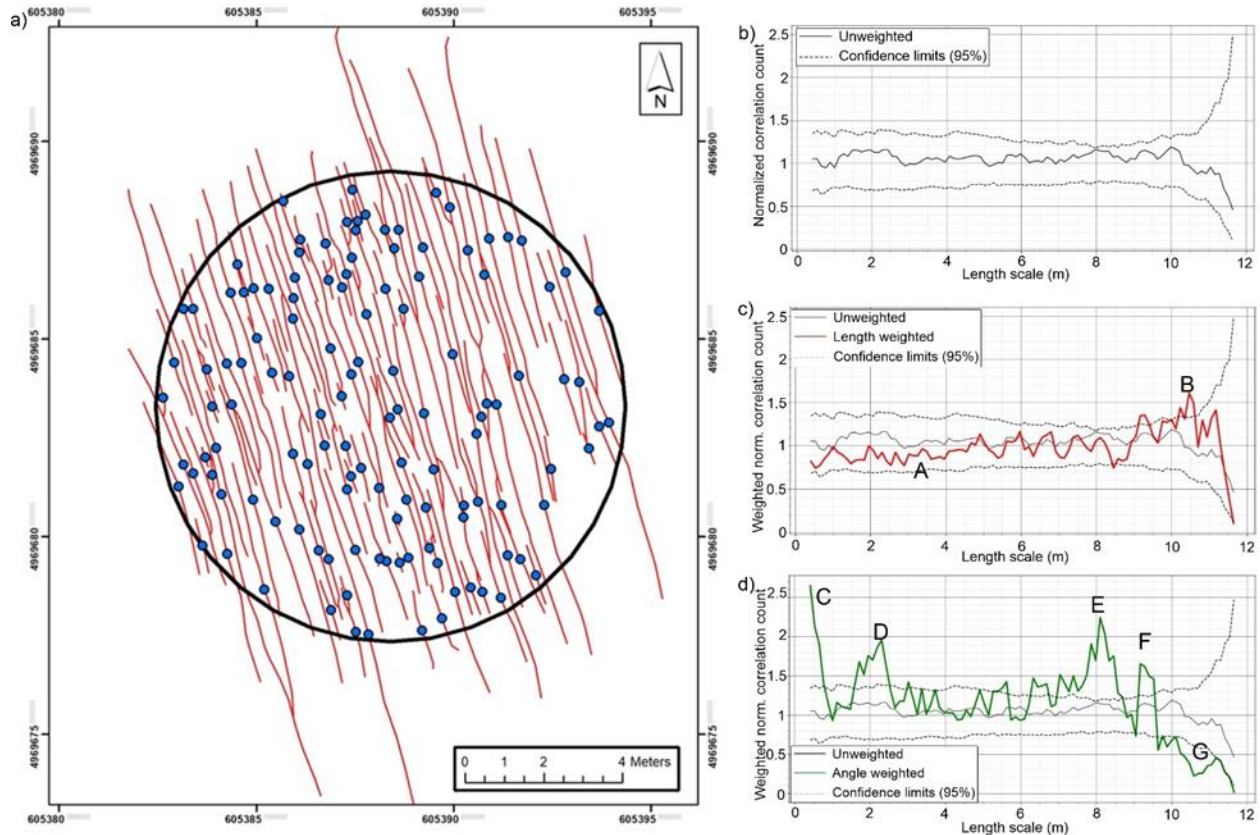
*Each microfracture population was best-fit with power law, exponential, normal, and lognormal equations; relative quality of fit of each equation was evaluated using the chi-square error (e.g., Hooker et al., 2014). The fit producing the lowest error is the closest fit to the data. Numbers in bold are chi-square best fit.

4.3.5 Spatial Arrangement

4.3.5.1 Fracture Spacing

Overall, the 1D spatial analyses for both Sets A and D show anticlustered (regular or periodic) arrangements of fractures, distinguished with 95% confidence at small distances (~10 cm), while the 2D analysis for Set A reveals a random arrangement of fracture barycenters, likely reflecting the initial random distribution of starter flaws for fracture nucleation (Corrêa et al., 2022). In this scenario, the lack of organization indicates sporadic activation of flaws with no mechanical interaction during early fracturing. Mechanical interaction and inhibition of new

fractures would have begun through expanding stress shadows as fractures continued growing, creating the observed non-random anticlustering pattern along 1D scanlines. The resulting mechanical interactions among growing fractures also promoted the development of longer fracture traces at regular distances ($> 9\text{m}$) and eventual hard linkage causing variability in strike at certain length scales.

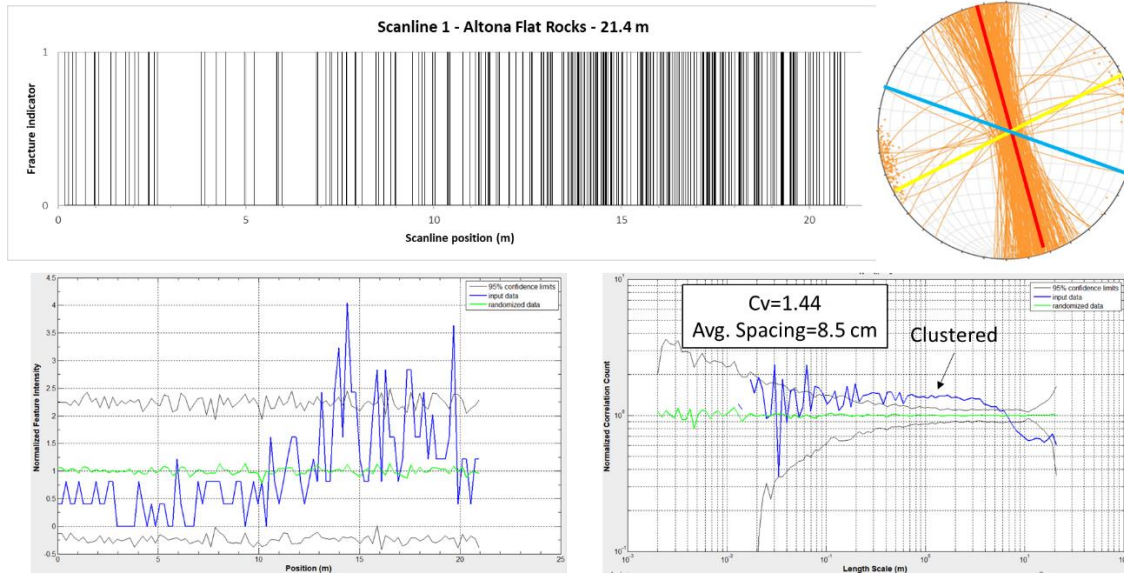


Supplementary Figure S2. Map showing N-S fracture traces and barycenters from Rt16 outcrop. Unweighted and weighted 2D NCC plots are shown on the right (from top to bottom: Unweighted, Length weighted, Orientation weighted), suggesting a random distribution of barycenters, long fractures at long distances ($> 9\text{m}$), and parallel orientation but dispersed (< 5 degrees) at a few selected distances. Shown with permission from (Corrêa et al., 2022).

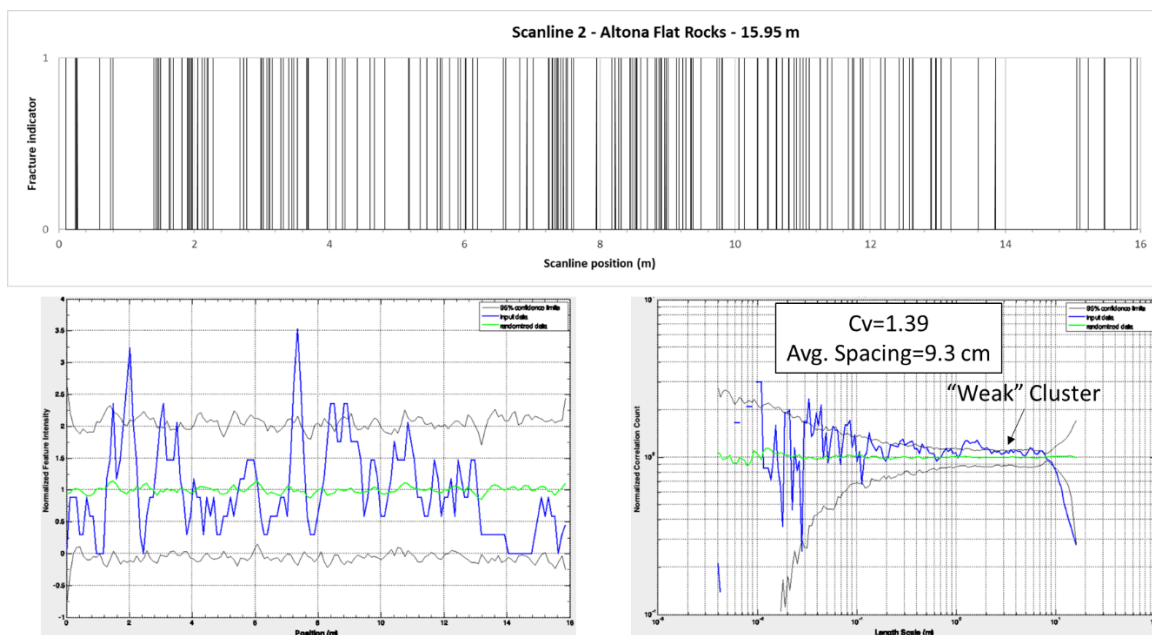
Brunell Road (BR) 1D Scanlines. All fractures at high angle to scanlines were measured, regardless of set.



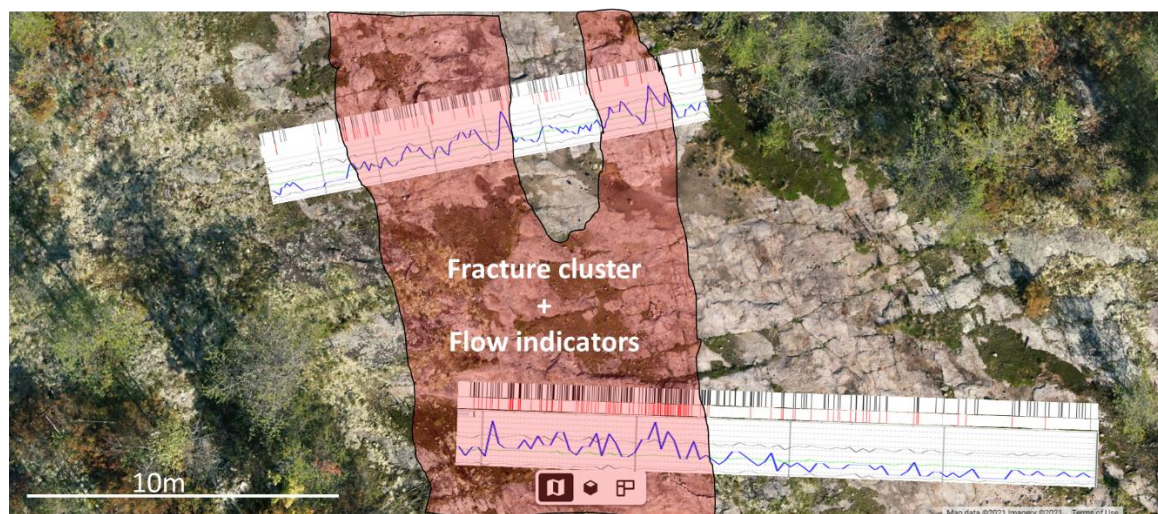
Supplementary Figure S3. We acquired data from two scanlines at Brunell Rd (BR) outcrop (see Table 3). Both scanlines are oriented approximately E-W and are around 10 m apart. We measured orientation and positions of fractures, as well as oxide staining along the entire scanline trace. Oxide staining in fractures are usually indicators of paleo flow (see Supplementary Figure S6).



Supplementary Figure S4. BR Scanline 1 was acquired in the south part of the outcrop. We found three fracture sets: NNW, NW, and NE striking. The distribution of fractures along the scanline is irregular with a high CV of 1.44 and average spacing of 8.5 cm. 1D NCC analysis also showed clustering as the curve plots above the confidence interval for several length scales forming a plateau. The fracture intensity plot shows a region of high fracture intensity from 13-21.4 m.



Supplementary Figure S5. BR Scanline 2 was acquired in the north part of the outcrop. The distribution of fractures is more regular as the lower CV of 1.39 suggests, with an average spacing of 9.3 cm. The NCC analysis supports the interpretation of clusters because the curve is just on top of the confidence limits. Moreover, the position just above the confidence limits suggests “weak clustering”. The intensity plot shows regions of high fracture intensity from 1-4 m and from 7-10 m.



Supplementary Figure S6. Stick plots and interpretation of cluster positions. Because both scanlines show fracture clusters aligned to each other and with flow indicators, we believe these clusters were probably part of a permeable fracture network present in the Potsdam Sandstone sometime in the past. The fracture clusters could have been important features enhancing flow in this location, as most of the stained fractures are within the clusters, suggesting they contributed to fluid flow. On Scanlines: Black ticks, fracture position; Red, Staining; Blue curve, fracture intensity.

4.3.6 Fluid Inclusion Microthermometry

Results of microthermometric analysis of two-phase aqueous fluid inclusions in Set A microfractures, Flat Rocks outcrop, Altona, New York. The fluid inclusions homogenize to the liquid field in a narrow range of 120 to 129°C and indicate the presence of a relatively high salinity fluid of approximately 20.0 to 21.5 wt% NaCl equivalents.

References

- Allmendinger, R. W., and Karabinos, P. (2023). Illuminating geology in areas of limited exposure using texture shading of lidar digital terrain models. *Geosphere*, 19(1), 163-178.
- Aydin, A., and Basu, A. (2005). The Schmidt hammer in rock material characterization. *Engineering geology*, 81(1), 1-14.
- Corrêa, R.S., Marrett, R., and Laubach, S.E. (2022). Analysis of spatial arrangement of fractures in two dimensions using point process statistics. *Journal of Structural Geology*, 163, 104726.
- Fall, A., and Bodnar, R. (2018). How precisely can the temperature of a fluid event be constrained using fluid inclusions? *Economic Geology* 113(8), 1817–1843. doi.org/10.5382/econgeo.2018.4614
- Forstner, S.R. and Laubach, S.E. (2022). Scale-dependent fracture networks. *Journal of Structural Geology* 165, 104748. doi.org/10.1016/j.jsg.2022.104748
- Gillespie, P.A., Walsh, J.J., Watterson, J., Bonson, C.G., and Manocchi, T. (2001). Scaling relationships of joint and vein arrays from The Burren, Co. Clare, Ireland. *Journal of Structural Geology* 23, 183–201.
- Goldstein, R.H., and Reynolds, T.J. (1994). Systematics of fluid inclusions in diagenetic minerals. Society for Sedimentary Geology Short Course 31, SEPM (Society for Sedimentary Geology), Tulsa, Oklahoma, 199 p.
- Gomez, L.A., and Laubach, S.E. (2006). Rapid digital quantification of microfracture populations. *Journal of Structural Geology* 28, 408–420.
- Götze, J., Plötze, M., and Habermann, D. (2001). Origin, spectral characteristics and practical applications of the cathodoluminescence (CL) of quartz—a review. *Mineralogy and Petrology* 71(3-4), 225–250.
- Healy, D., Rizzo, R.E., Cornwell, D.G., Farrell, N.J., Watkins, H., Timms, N.E., Gomez-Rivas, E., and Smith, M. (2017). FracPaQ: A MATLAB™ toolbox for the quantification of fracture patterns. *Journal of Structural Geology* 95, 1–16. doi.org/10.1016/j.jsg.2016.12.003
- Hooker, J.N., Marrett, R., and Wang, Q. (2023b). Rigorizing the use of the coefficient of variation to diagnose fracture periodicity and clustering. *Journal of Structural Geology* 168, 104830. doi.org/10.1016/j.jsg.2023.104830
- Kastner, M., and Siever, R. (1979). Low temperature feldspars in sedimentary rocks. *American Journal of Science* 279(4), 435-479.
- Katz, O., Reches, Z., and Roegiers, J.C. (2000). Evaluation of mechanical rock properties using a Schmidt Hammer. *International Journal of Rock Mechanics and Mining Sciences* 37(4), 723–728.
- Lander, R.H., and Walderhaug, O. (1999). Porosity prediction through simulation of sandstone compaction and quartz cementation. *AAPG Bulletin* 83, 433–449.
- Lundegard, P.D. (1992). Sandstone porosity loss; a “big picture” view of the importance of compaction. *Journal of Sedimentary Research* 62(2), 250–260.
- Marrett, R., Gale, J.F.W., Gomez, L., and Laubach, S.E. (2018). Correlation analysis of fracture arrangement in space. *Journal of Structural Geology* 108, 16–33. doi.org/10.1016/j.jsg.2017.06.012
- Milliken, K.L., and Laubach, S.E. (2000). Brittle deformation in sandstone diagenesis as revealed by scanned cathodoluminescence imaging with application to characterization of fractured reservoirs (Chapter 9). In M. Pagel, V. Barbin, P. Blanc, D. Ohnenstetter, eds.,

- Cathodoluminescence in Geosciences, Springer Verlag, Springer, Berlin, Heidelberg, 225–243. doi.org/10.1007/978-3-662-04086-7_9
- Milliken, K.L., Reed, R.M., and Laubach, S.E. (2005). Quantifying compaction and cementation in deformation bands in porous sandstones. In R. Sorkhabi, Y. Tsuji, eds., *Faults, Fluid flow, and Petroleum Traps*, AAPG Memoir 85, 237–249.
- Ortega, O.J., Marrett, R., and Laubach, S.E. (2006). A scale-independent approach to fracture intensity and average spacing measurement. *AAPG Bulletin* 90(2), 193–208.
- Paxton, S.T., Szabo, J.O., Ajdukiewicz, J.M., and Klimentidis, R.E. (2002). Construction of an intergranular volume compaction curve for evaluating and predicting compaction and porosity loss in rigid-grain sandstone reservoirs. *AAPG Bulletin* 86(12), 2047–2067.
- Sanderson, D.J., and Nixon C.W. (2015). The use of topology in fracture network characterization. *Journal of Structural Geology* 72, 55–66.
- Selleck, B.W. (1997). Potsdam Sandstone of the southern Lake Champlain Valley: Sedimentary facies, environments and diagenesis: *New England Intercollegiate Geology Conference*, Field Trip Guidebook, pC3-1–16.
- Stokes, D.J. (2008). *Principles and Practice of Variable Pressure/Environmental Scanning Electron Microscopy (VP-ESEM)*. John Wiley and Sons, West Sussex, 221 p., ISBN780470065402
- Terzaghi, R.D. (1965). Sources of error in joint surveys. *Geotechnique* 15(3), 287–304.
- Thompson, S.K. (1987). Sample size for estimating multinomial proportions. *The American Statistician* 41(1), 42–46.
- Wennberg, O.P., Casini, G., Jonoud, S., and Peacock, D. C. (2016). The characteristics of open fractures in carbonate reservoirs and their impact on fluid flow: a discussion. *Petroleum Geoscience* 22(1), 91–104.